Made available through a Creative Commons CC-BY License

THE JOURNAL OF PHYSICAL CHEMISTRY C

ACS AUTHORCHOICE

pubs.acs.org/JPCC Article

Defects in the Amorphous–Crystalline Evolution of Gel-Derived TiO_2

C. Koral, M. Fantauzzi, C. Imparato, G. P. Papari, B. Silvestri, A. Aronne, A. Andreone,* and A. Rossi*

Cite This: J. Phys. Chem. C 2020, 124, 23773–23783

Read Online

ACCESS | Metrics & More | Article Recommendations | Supporting Information

ABSTRACT: The catalytic and electro-optical properties of TiO_2-based materials depend on the defectivity of their electronic structures and in turn on the synthesis conditions. It is however less clear how to control the number of defects in this oxide. In this paper, spectroscopic and structural characterization of chemical [acetylacetonate–TiO_2, hybrid gel, hybrid sol–gel titania (HSGT)] and particulate [inorganic gel, sol–gel titania (SGT)] TiO_2 amorphous gels is presented. HSGT and SGT were thermally treated at different annealing temperatures and at various times, obtaining anatase or rutile samples. X-ray diffraction, X-ray photoelectron spectroscopy (XPS), and terahertz-time domain spectroscopy (THz-TDS) were exploited for monitoring changes in the crystallographic structure, chemical composition, and dielectric function. It is found that the thermal treatment affects in different ways the hybrid and the particulate TiO_2 gels, resulting in an increase of electron transfer in the former. Moreover, XPS combined with X-ray-induced Auger electron spectroscopy provides evidence that the ionicity of the bond is also different and well correlates with the number of defects. These results demonstrate that XPS and THz-TDS techniques can be used as complementary tools for determining the electronic properties of titania with various degrees of crystallinity and defects.

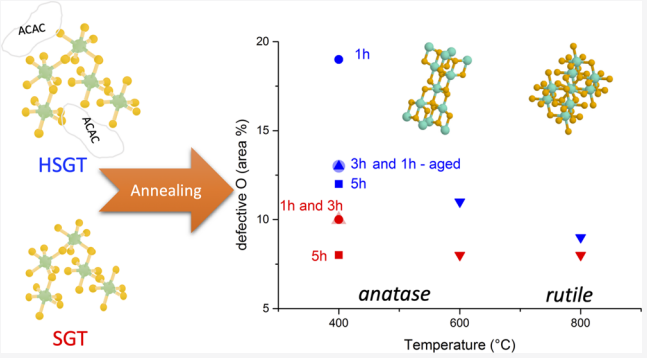

1. INTRODUCTION

Titanium dioxide (TiO_2) is an extensively known wide band-gap semiconductor with enormous potential for both industry and material science due to its peculiar catalytic and electro-optical properties.[1] Its functionality in a wide range of applications, such as photocatalysis, environmental remediation, solar cells, and molecular sensing, can be enhanced by engineering the defectivity of its electronic structure. In fact, the presence of intrinsic defects, in particular oxygen vacancies or reduced Ti sites (Ti^{3+} with self-doping effect), significantly affects the charge transport, radiation absorption, and surface reactivity of TiO_2.[2,3] Such defects represent active surface sites for the interaction with target compounds and reactants and/or act as electron-trapping sites, improving the photoinduced charge separation lifetime. Moreover, the nature of TiO_2 phase (amorphous, anatase, rutile, etc.) and therefore the synthesis methodology play a key role in defining the suitability for specific applications.

TiO_2 with an appropriate distribution of defects can be obtained by diverse synthetic strategies; among them, the sol–gel technique is widely used due to its cost effectiveness, processing simplicity, large-scale production capability, and versatility.[4,5] The sol–gel synthesis of TiO_2 particles usually starts with the hydrolysis of a titanium precursor, giving rise either to the precipitation of titanium oxo-hydroxide (a physical gel) or to the formation of chemical gels (interconnected networks of solid and liquid phases). Homogeneous gelation produces porous bulk materials with a finely controlled composition and uniform structure on the molecular scale. Its achievement requires the modulation of hydrolysis and condensation rates through the careful choice of synthesis conditions and the use of complexing organic molecules.

By this approach, we obtained TiO_2 hybrid amorphous chemical gels [hybrid sol–gel titania (HSGT)] with the addition of acetylacetone as a complexing ligand during the synthesis procedure.[6−8] The process of drying wet hybrid gels in air produced xerogels characterized by (i) visible-light absorption, (ii) some extent of Ti^{3+}-self doping, (iii) an extraordinary ability to generate and stabilize superoxide radical anions on their surface, owing to the presence of acetylacetonate ligands, which promotes the formation of oxygen vacancies and then the adsorption and reduction of O_2, and (iv) a consequent activity in the degradation of organic pollutants in water without light irradiation.[6−8] The unusual long-term stabilization of reactive oxygen species on these amorphous hybrid materials opens perspectives for a broad

Received: August 19, 2020
Revised: September 27, 2020
Published: October 20, 2020

Downloaded via UNIV OF CAGLIARI on December 5, 2024 at 08:38:49 (UTC).
See https://pubs.acs.org/sharingguidelines for options on how to legitimately share published articles.

© 2020 American Chemical Society

https://dx.doi.org/10.1021/acs.jpcc.0c07568
J. Phys. Chem. C 2020, 124, 23773–23783

range of applications involving oxidative processes. Furthermore, by drying wet hybrid gels under vacuum and subsequent thermal treatments in different atmospheres, we obtained anatase TiO_2/C bulk heterostructures showing a remarkable photocatalytic activity in hydrogen generation.[9] All these peculiar features are strictly related to the organic component in HSGT and are not observed on particulate amorphous TiO_2 gels [sol−gel titania (SGT)] prepared following a similar procedure but without any additives.

In the structural investigation of TiO_2-based materials, X-ray photoelectron spectroscopy (XPS) was traditionally used for the identification of defective sites such as reduced titanium,[10,11] defective oxygen,[1,10−13] as well as for the analysis of the electronic structure based on the valence band spectra[14] and dopants.[15] On the other hand, terahertz-time domain spectroscopy (THz-TDS) has evolved in recent years into an excellent tool for the characterization of the electrodynamic properties of bulk nanometer-sized materials.[16,17] By using this technique, the transient THz electric field propagating inside a sample is detected in terms of both its amplitude and phase. The constituent elements of the pulse are directly connected with the absorption coefficient and the refractive index and in turn with the effective conductivity and permittivity of the material, which can be measured with high accuracy. Recently, several studies exploited THz-TDS to investigate the electron transport, the optical and conductivity properties of nanostructured TiO_2.[18,19] Nevertheless, only a few reports dealt with both XPS and THz-TDS for the characterization of metal oxides,[9,20−22] and in those papers, the spectroscopic tools were used separately in order to address specific questions about the surface composition and the electrodynamic properties. It is worth noting that a correlation between the results obtained by the two techniques was not attempted so far.

Here, for the first time, a thorough analysis of TiO_2 was performed by combining XPS and THz-TDS, aiming to emphasize the complementarity of these only apparently far techniques with special attention to surface and electro-optical properties, following the structural evolution of air-dried HSGT and SGT xerogels from the amorphous state to anatase and rutile phases. In addition, a more detailed XPS analysis involving the so-called chemical state plot[23,24] and the exploitation of X-ray-induced Auger lines[25−28] also provides valuable information on the ionicity and covalency of the chemical bonds and the dielectric properties of the analyzed materials. Indeed, following photoemission, the molecular environment responds to the creation of the core hole and the energy gain due to this effect, called extra-atomic relaxation energy, depends on polarization effects. The polarization energy, related to the extra atomic relaxation energy, would be larger for more conductive materials than for insulators.

2. EXPERIMENTAL SECTION

2.1. Sol−Gel Synthesis. TiO_2 samples were synthesized by two hydrolytic sol−gel procedures carried out at room temperature and described in previous works[6,7] using titanium(IV) *n*-butoxide (97+%), acetylacetone (2,4-pentanedione, Hacac) (99+%), 1-propanol (99.80%), and hydrochloric acid (37 wt %) provided by Sigma-Aldrich.

In the standard sol−gel procedure, a solution of Ti(IV) *n*-butoxide and 1-propanol was prepared; then a solution of 0.1 mol/L HCl in bidistilled water and 1-propanol was added to the first one under stirring, giving molar ratios Ti/1-propanol/H_2O = 1:5:10. The result was the fast formation of a white particulate gel (SGT, sol−gel titania).

The hybrid sol−gel procedure is distinguished by the introduction of acetylacetone into the Ti(IV) *n*-butoxide solution, with final molar ratios Ti/Hacac/1-propanol/H_2O = 1:0.4:5:10. After the addition of the HCl/water/1-propanol solution, a homogeneous and yellowish albeit transparent gel was formed in a few minutes (HSGT, hybrid sol−gel titania). The addition of a suitable amount of acetylacetone, a diketone acting as chelating ligand for Ti^{4+} ions, directs the system to a chemical gel that after drying results in a coarse-grained xerogel.

After ageing under ambient conditions for 1 day, the wet gels were dried in a ventilated oven at 50 °C. The dried gels, indicated as SGT and HSGT, were ground in a mortar prior to characterization and thermal treatments. Both dried samples were subjected to thermal treatment in air at different temperatures and times, in a tubular furnace with 10 °C/min heating rate. A set of samples was annealed for 1 h at 400, 600, and 800 °C a second set was annealed at 400 °C for different times: 1, 3, and 5 h. They are named SGT-*x*-*y* and HSGT-*x*-*y*, where *x* is the treatment temperature (in °C) and *y* is the treatment duration (in hours).

2.2. Materials Characterization and Data Processing. X-ray diffraction (XRD) measurements were performed with a Philips X'Pert-Pro diffractometer by using monochromatic Cu Kα radiation (40 mA, 40 kV) with a step width of 0.013° 2θ. The average size of TiO_2 crystallites was evaluated by the Scherrer's equation taking the full width at half-maximum of the most intense diffraction peak. The fraction of amorphous, anatase, and rutile phases were estimated by the integration of XRD profiles, considering the area of the diffraction peaks related to the crystalline phases and that of the broad amorphous halo.

Field emission scanning electron microscopy (FESEM) images were acquired by a FEI Nova NanoSEM 450 emission SEM at an accelerating voltage of 5 kV, equipped with an Everhart−Thornley detector and a through-lens-detector after sputter coating of the samples with a thin layer of Au−Pd alloy for preventing charging of the surface.

X-ray photoelectron spectra were acquired using a PHI Quantera SXM (ULVAC-PHI, Chanhassen, MN, U.S.A.). The powders were analyzed using a monochromatic Al Kα source ($h\nu$ = 1486.6 eV), and the analyzer was operated in the fixed analyzer transmission mode. The survey spectra were recorded setting the pass energy at 280 eV and the step size at 1 eV, whereas the high-resolution spectra were acquired setting the pass energy at 69 eV and the step size at 0.05 eV. Periodic check of the linearity of the binding energy (BE) scale was performed according to ISO 15472:2010 and the accuracy was found to be 0.1 eV. The electron neutralizer was used during the analyses in order to compensate for sample charging and the BEs were further corrected with reference to aliphatic carbon taken at 285.0 eV. More information on the data processing and instrument characteristics are provided elsewhere.[9]

Samples for terahertz spectroscopy were prepared as pellets using SGT and HSGT sample series finely ground powders. Because of their fragile nature, to increase the mechanical strength and for easy handling of the pellets during the spectroscopic investigation, the powders were pressed in between two supporting holed paper disks having 0.5 and 1 cm inner and outer diameter. This method allows reducing the

https://dx.doi.org/10.1021/acs.jpcc.0c07568
J. Phys. Chem. C 2020, 124, 23773−23783

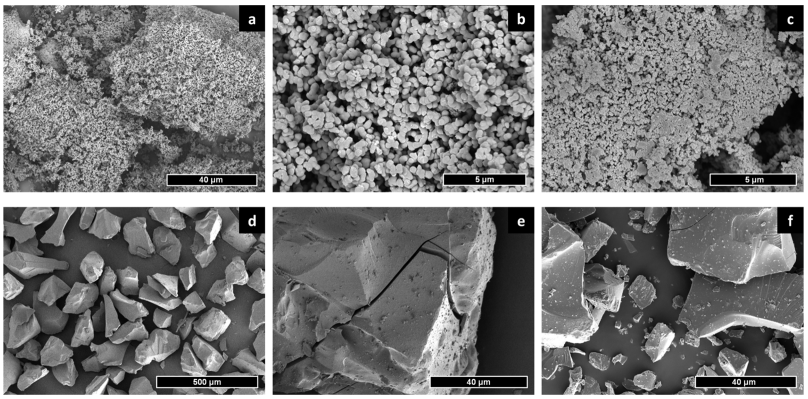

Figure 1. SEM images at different magnifications of SGT (a,b) and HSGT (d,e) dried gels, and of SGT-400-1 (c) and HSGT-400-1 (f). Scale bar (a,e,f) 40; (b,c) 5; (d) 500 μm.

Table 1. Annealing Conditions, Crystalline Phase, Average Crystallite Size (Estimated by Scherrer's Equation), and Fraction of Amorphous Phase for All Studied TiO_2 Samples

sample	annealing T (°C)	annealing time (h)	crystalline phase	crystallite size (nm)	amorphous phase (%)
SGT			amorphous		100
SGT-400-1	400	1	anatase	8	25
SGT-400-3	400	3	anatase	9	23
SGT-400-5	400	5	anatase	9	15
SGT-600-1	600	1	anatase	23	13
SGT-800-1	800	1	rutile (95%)	55	
			anatase (5%)	43	
HSGT			amorphous		100
HSGT-400-1	400	1	anatase	9	28
HSGT-400-3	400	3	anatase	9	25
HSGT-400-5	400	5	anatase	12	17
HSGT-600-1	600	1	anatase	30	
HSGT-800-1	800	1	rutile	68	

surface fracturing and gives pellets with relatively homogeneous thickness (about 0.2 mm). Prior to the electro-optical study, the void percentages of each pellet were measured by evaluating the densities based on the dimensions and mass of the samples.[9,19,20] The relative density of prepared pellets was estimated based on reported crystallographic densities of anatase (3.8 g/cm^3) and rutile (4.2 g/cm^3) TiO_2[3] and assuming 3.0 g/cm^3 for the amorphous samples because of their considerable content of organic components and adsorbed water (up to 20 and 30 wt % in SGT and HSGT dried gels, respectively).

A custom-built THz spectrometer driven by a 100 fs Nd:YAG laser source was used for all measurements. Photoconductive antennas were employed for THz generation and detection. Off-axis parabolic metal reflectors were used along the optical path to collimate and focus the broad THz frequency range onto the pellets placed concentrically on a metal iris with 5 mm aperture. Spot size of the THz beam was measured to be around 3 mm.

A detailed description of the measurement scheme has been reported elsewhere.[29] Basically, the time-dependent pulsed electric field transmitted through the sample (E_s) and through the free space (E_r, reference signal) is acquired separately. Then, the temporal profiles are converted into the frequency domain by applying a standard fast Fourier transform technique, and the material transfer function $T(\omega) = E_s/E_r$ is derived. T correlates with the signal amplitude and phase changes due to the absorption and refraction processes in each sample. The frequency-dependent complex index of refraction $\tilde{n}(\omega) = n(\omega) + ik(\omega)$ is extracted by means of a commercial software that uses a total variation technique to iteratively minimize the periodic Fabry–Perot oscillations produced inside the target.[30] This quantity can be directly correlated with the complex dielectric function $\tilde{\varepsilon}(\omega) = \varepsilon'(\omega) + \varepsilon''(\omega)$ using the given relations: $\varepsilon' = n^2 - k^2$ and $\varepsilon'' = 2nk$.

3. RESULTS AND DISCUSSION

3.1. Structural Characterization. Depending on the addition of acetylacetone as complexing ligand, the products of the sol–gel synthesis are visibly different, as confirmed by SEM images: the SGT white samples appear as loosely aggregated spherical particles with diameter of a few hundred nm (Figure 1a,b). Conversely, the HSGT xerogel (Figure 1d,e) is a bulk granular material, yellow-colored because of the ligand-to-metal charge transfer complex between acetylacetonate and Ti.[6] Its particle size can be therefore selected in the desired range (tens to hundreds of μm) by grinding and sieving. A thermal treatment at 400 °C for 1 h appears to enhance the partial aggregation of SGT powders (Figure 1c) and could cause some fragmentation of HSGT particles (Figure 1f), but it does not substantially alter the morphology of the two materials. All samples were analyzed by powder XRD (Figure S1). The crystalline phase and average crystallite size estimated from these data are reported in Table 1. Both gels are amorphous when dried under ambient conditions at low temperature (lower than 50 °C). Crystallization starts

https://dx.doi.org/10.1021/acs.jpcc.0c07568
J. Phys. Chem. C 2020, 124, 23773–23783

Table 2. Evaluated O/Ti Atomic Ratio, BE of Ti 2p, KE of X-ray-Induced Auger Signal Ti LMM, Auger Parameter and Extra-Atomic Relaxation Energy

sample	O/Ti	Ti $2p_{3/2}$ (eV ± 0.1)	Ti LMM (eV ± 0.2)	$BE_{Ti\ 2p}$ + $KE_{Ti\ LMM(eV)}$ (eV ± 0.2)	ΔR^{ea}_{T-am} (eV)
SGT[7]		459.2 (IV)	412.8	872.0 (IV)	
		457.4 (III)		870.2[a] (III)	
SGT-400-1[7]		459.1	413.4	872.5	0.25
SGT-400-3	2.0 (0.1)	459.1	413.6	872.7	0.35
SGT-400-5	1.9(0.1)	459.0	413.6	872.6	0.3
SGT-600-1	2.0 (0.1)	459.0	413.7	872.7	0.35
SGT-800-1	2.0 (0.1)	459.0	414.0	873.0	0.5
HSGT[7]		459.0 (IV)	412.9	871.9 (IV)	0
		457.1 (III)		870.0 (III)[a]	
HSGT-400-1[7]		459.3 (IV)	413.2	872.5 (IV)	0.3
		457.3 (III)		870.5 (III)[a]	
		455.8 (sub ox)		869.0 (sub)[a]	
HSGT-400-1 aged[9]	2.0 (0.1)	458.9	413.9	872.8	0.45
HSGT-400-3	2.0 (0.1)	458.9	413.9	872.8	0.45
HSGT-400-5	1.9 (0.1)	459.0	413.9	872.9	0.5
HSGT-600-1	1.98 (0.1)	459.0	413.7	872.7	0.4
HSGT-800-1	2.0 (0.1)	458.9	414.3	873.2	0.65

[a]Calculated taking into account the KE of the centroid of Ti LMM line (column Ti LMM).

occurring into the anatase phase upon annealing at 400 °C. It is clearly observed that increasing the annealing time up to 5 h does not produce a discernible effect on the substantial growth of the crystals, except for HSGT-400-5. Rather, a longer thermal treatment fosters the advancement of the crystallization of the residual amorphous phase.

A consistent crystallite growth is observed only at 600 °C, being faster in HSGT than in SGT samples. At the highest temperature (800 °C), the anatase-to-rutile transition is practically complete. Only SGT-800 includes a 5% residual anatase phase. Both the crystallization of amorphous TiO_2 and the anatase-to-rutile transformation are reported to occur in wide temperature ranges, mainly depending on the synthesis method and conditions.[5] The presence of point structural defects, such as vacancies, is known to facilitate the phase transition, acting as heterogeneous nucleation sites. In HSGT, a higher concentration of these defects originated from the removal of the organic component and the larger particle size may favor the growth of rutile grains.

It is essential to note that the differences between the properties of the prepared materials are not limited to the dried samples but persist after thermal treatments that remove acetylacetonate from HSGT. SGT-400-1 is almost stoichiometric TiO_2, whereas HSGT-400-1 shows a marked surface sub-stoichiometry, with a high fraction of reduced Ti, as evidenced by XPS analysis.[7] This result is attributed to the relatively reducing conditions generated by the release of organics and adsorbed superoxide radicals from the hybrid xerogel. The defective structure of HSGT-400-1 is reflected in its extended visible-light absorption (dark gray coloration) and its electron paramagnetic resonance (EPR) spectrum recorded at room temperature, showing a peak assigned to single electrons trapped in oxygen vacancies (F^+ centers), with a possible contribution from radicals localized on carbon species derived from the organic ligand.[7,9] On the other hand, SGT-400-1 gives no EPR signal. A longer annealing in air is supposed to promote surface re-oxidation. In fact, HSGT-400-3 already shows a lighter gray color and a strongly decreased intensity of the EPR peak,[9] while HSGT-400-5 appears almost white and EPR-silent, indicating a gradually reduced amount of point defects, in agreement with XPS data. The same is observed by heating this hybrid at a higher temperature (HSGT-600-1): in the presence of O_2, vacancies are compensated and residual carbon impurities are combusted. Moreover, the marked Ti^{3+}-self doping observed for the HSGT-400-1 as-prepared sample was not retained after aging for about 2 years.[9] It is evident that the formation and stabilization of a defective structure starting from the hybrid gel is allowed in a specific and restricted range of annealing conditions.

3.2. Surface Characterization. XPS analyses allow calculating the composition of the samples and upon annealing almost stoichiometric TiO_2 is obtained (Table 2).

The Ti 2p signal for all examined samples exhibits a doublet due to spin orbit coupling (Figure S2). Following the fitting strategy proposed elsewhere,[7] the components due to Ti(IV), Ti(III), and Ti sub-oxides are considered for the Ti 2p curve fitting. In these series of samples, reduced Ti species, whose signals are expected to be at about 457 and 456 eV, are hardly detected (aged samples). The BE value of the Ti(IV) component is given in Table 2 for all samples and for comparison; data from the ref 7 are also provided.

BE values of Ti $2p_{3/2}$ component are typical for Ti-(IV),[7,31−34] and a small shift toward lower values increasing the temperature and thus the crystallite size is observed for the HSGT series. A similar shift was observed in iron oxides[28] and ascribed to differences in the ionicity of the metal−oxygen bonds. Such a difference might also be detected on the Ti LMM X-ray-induced Auger signals.

In Figure S2, the Ti LMM spectra of the samples analyzed in this paper and, for comparison, the spectra recorded on the samples analyzed in ref 7 and on the aged HSGT-400-1 sample[9] are shown. It is possible to observe a significant shift of the peaks toward high kinetic energy (KE) values, increasing the temperature and thus the crystallites size for both the SGT and HSGT series, even if more pronounced for the latter. The combination of photoelectron and X-ray-induced Auger lines provide useful information for the identification of the chemical state of the elements. The Auger parameter $\alpha' = BE_{Ti\ 2p} + KE_{Ti\ LMM}$ is calculated for all samples under test and

https://dx.doi.org/10.1021/acs.jpcc.0c07568
J. Phys. Chem. C 2020, 124, 23773−23783

for comparison also for samples analyzed in ref 7 and the aged HSGT-400-1.[9] α' values are reported in Table 2.

The BE of Ti 2p is typical for Ti(IV) leaving no doubts on the oxidation state of Ti in our samples. However, the pronounced shift in the KE of Ti LMM provides further information, especially when combined with the chemical state plot (Figure 2). The chemical state plot, or Wagner plot, includes the BE, KE, and α' information for an element.[23]

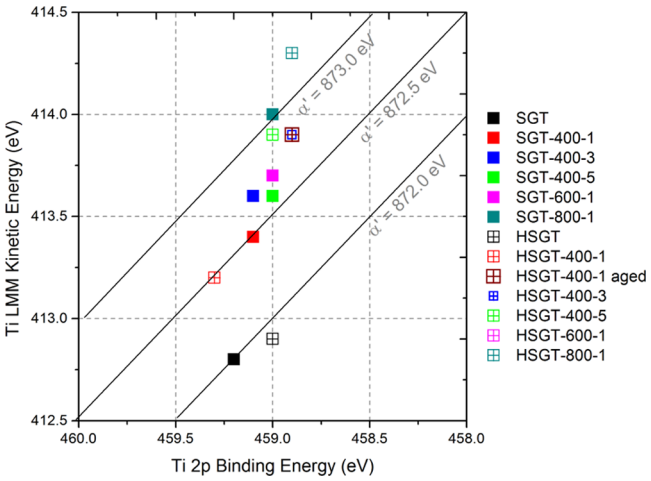

Figure 2. Ti chemical state plot.

In a chemical state plot, the KE (eV) of the Auger lines for an element in different compounds is plotted versus the BE of the photoelectron lines. The points on lines with slope −1 have the same Auger parameter and thus the same chemical state. The position of the points in the plot can be rationalized in terms of initial and final state effects. All samples show small differences in the BE values. The KE values of Ti LMM increase with the annealing time and temperature, leading to high values of Auger parameter.

Both the crystallite size and the percentage of crystalline phases increase with the annealing temperature (Table 1). According to several authors,[28,34,35] size effects may affect Auger parameter values and the position of the points in the Wagner plot.

Both the shift in BE (ΔBE) and in KE (ΔKE) values are due to initial (ΔV) and final (ΔR^{ea}) state effects, according to the equations[24]

$$\Delta BE = \Delta V - \Delta R^{ea} \quad (1)$$

$$\Delta KE = -\Delta V + 3\Delta R^{ea} \quad (2)$$

Among the initial state effects, the formal oxidation state and the Madelung potential, which affect the orbital energy of the un-ionized atom before photoemission, have to be considered.[24] Following photoemission, the molecular environment responds to the creation of the core hole, and the energy gain due to this effect (ΔR^{ea}, extra-atomic relaxation energy) depends on polarization effects.

The shift in the Auger parameter values depends on the extra atomic relaxation energy, since

$$\Delta\alpha' = \Delta BE + \Delta KE = 2\Delta R^{ea} \quad (3)$$

Both in SGT and HSGT samples, the BE shifts between the dried samples and the samples annealed at 800 °C are moderately small; nevertheless a KE shift of 1.0 and 1.3 eV is observed for the SGT and HSGT series, respectively. This result is typical for samples in which the initial and final state effects have similar values. In the following, the contribution of initial and final state effects on the XPS data is discussed.

3.2.1. Initial State Effects. Initial state effects might be due to differences in the Madelung potential and in the ionicity of Ti/O bonds.

Since the higher annealing temperature determines an increase of the crystallite size, the number of Ti(IV) in the second coordination shell of Ti in annealed samples increases with temperature,[35] leading to a more positive Madelung potential than in the dried ones. This change results in the presence of the data points in the upper part of the Wagner plot.

As far as the ionicity of the Ti/O bond is concerned, the lower the KE of Ti LMM, the higher is the ionicity, in agreement with ref 27; therefore, the Ti/O bonds in SGT and HSGT dried gels are more ionic than in the annealed samples.

To further substantiate this result, the O KLL spectra are also considered (Figure S3 and Table S1) since in ref 26 the energy separation between O $KL_{23}L_{23}$ and O KL_1L_{23} and the intensity ratios of those two peaks are related to metal−oxygen ionicity. In detail, highly ionic oxides such as MgO showed higher values for the intensity ratio and lower energy differences than less ionic oxides, such as SiO_2. The energy separation and the intensity ratios are plotted against the annealing temperature for SGT and HSGT samples in Figure S4a,b. Since the energy separation increases and the intensity ratio decreases with annealing time, it is confirmed that the ionicity of Ti/O bonds decreases, increasing the crystallite size (samples annealed at higher T) and the different ionicity affects the Ti Auger parameter values.

3.2.2. Final State Effects. Since the Auger parameter shift, which is an empirical estimation of the extra-atomic relaxation energy, depends on the polarizability of the chemical environment of the core-ionized atom, it also depends on several physical quantities related to the polarizability, such as the refractive index and the dielectric constant at the optical frequencies (ca. 10^{15} Hz).[24]

The extra-atomic relaxation energy increases with the annealing temperature. It is interesting to observe that the point due to the aged HSGT-400-1 sample falls in the same position as the data point due to HSGT-400-3, confirming that the presence of reduced Ti species in HSGT-400-1 determines differences in the relaxation of the primary core-hole caused by photoemission and consequently in polarizability of the ligands. The XPS spectra of the aged sample did not show the presence of Ti^{3+}, and the sample exhibited the same chemical state of the one thermally treated at 400 °C for 3 h (HSGT-400-3). This finding suggests that heat treatment and aging result in HSGT evolving to a less defective material.

In Table 2, we report the ΔR^{ea}_{T-am}, defined as the extra-atomic relaxation energy difference between annealed and amorphous samples. In Section 3.4, we will show, using a simple electrostatic model, that ΔR^{ea}_{T-am} can be related to the local dielectric constant of both SGT and HSGT series and linked to the "bulk" dielectric response. This latter quantity will be retrieved from THz spectroscopy data in the next section, using a mean field analysis to take into account that samples are pellets with voids showing a non-Drude type behavior.

3.3. Electro-Optical Properties. The dielectric constant of a material is strongly influenced by its structural and morphological characteristics such as the crystallinity degree,

https://dx.doi.org/10.1021/acs.jpcc.0c07568
J. Phys. Chem. C 2020, 124, 23773−23783

grain size, and porosity. For titanium dioxide, the values of dielectric constants reported in the literature lie in a large range,[18,36] proving a strong dependence on the processing conditions and sample inhomogeneity. This stems from the uncontrolled mix of various phases, self-doping, and defects,[37] because of which the extracted dielectric functions (from the raw data sets) are found to be different than the well-studied static constants of the anatase and rutile TiO_2.[38] Analogous behavior was reported in many works dealing with samples investigated under similar conditions.[18,19,39,40]

The void percentage of sample pellets is evaluated according to the procedure described in the Experimental Section, giving the following average filling fractions: for the amorphous and anatase samples 0.60 (SGT) and 0.65 (HSGT) and for the rutile samples 0.65 (SGT) and 0.70 (HSGT). Void percentages show no discernible deviation with the diverse annealing temperature and duration in the anatase phase, whereas densification with the increased temperature is found to be more evident for the rutile phase samples. Moreover, pellets of HSGT synthesized powders are found to be slightly denser than those of SGT powders.

We retrieved the dielectric constants of each sample, considering first the void percentage and then the amorphous phase percentage (Table 1) under the mean field theory assumption by using the Landau−Lifshitz−Looyenga mixture model[41]

$$(\varepsilon)^{1/3} = \nu_1(\varepsilon_1)^{1/3} + \nu_2(\varepsilon_2)^{1/3} \tag{4}$$

ε represents the complex permittivity of the mixture, ε_1 is the permittivity of the host medium in which particles of permittivity ε_2 (guest medium) are dispersed, and ν_1 and ν_2 are the volume fractions of the respective components.

From a first analysis of the data as a function of frequency, we found that all samples present a dielectric function response departing from a standard Drude−Smith model.[42] Similar behavior is commonly observed in nanostructured media, including semiconductors[43] and oxides with relatively large grain boundaries, where charge transport mechanisms are dominantly affected by interface effects.

Carrier scattering processes at boundaries and local field effects on charge transport in nanostructured media have been well studied in the literature. The local depolarization fields and the charge localization and scattering are reported to be the main mechanisms determining the macroscopic response of the charge carriers in an inhomogeneous nanosystem.[44] On a length scale much smaller than the wavelength of the impinging radiation, where the carrier mean free path is comparable to the dimensions of the particles, the local field effects significantly dominate the electronic response of the system. In other words, stronger charge localization leads to an altered conductivity response.

A non-Drude type behavior of charge carrier dynamics of porous media is well studied in the literature, with non-trivial approaches (semi-quantum models, Monte Carlo simulations, ...) including the intragrain and intergrain transport contributions and, most importantly, the phononic response.[45] As a matter of fact, we observed a slightly parabolic increase in both real and imaginary parts of the dielectric function (Figure 3), which can be naturally explained as the onset of the phonon modes contribution to this part of the spectrum. Considering the possible large splitting between the transverse and longitudinal optical phonon frequencies in TiO_2, a classical harmonic oscillator model can be implemented for extracting

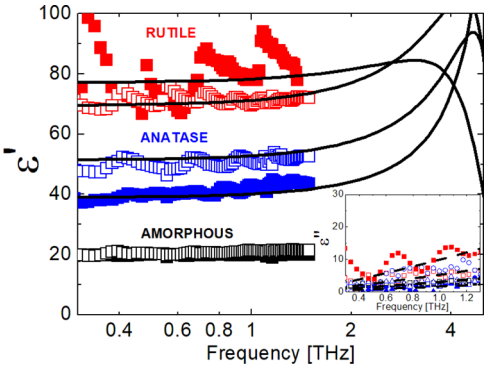

Figure 3. Real part of the measured dielectric function as a function of frequency (log scale). Full and empty square symbols refer to HSGT and SGT samples, respectively. Red, blue, and black color code is used for rutile, anatase, and amorphous phases. In the inset, using the same symbols, the imaginary part of the dielectric function as a function of frequency (linear scale) is shown. The corresponding DL oscillator model fits (applied to the polycrystalline samples only) are shown as solid (real part) and dashed (imaginary part) lines.

the dielectric constants in a frequency window relatively close to the resonance frequencies. Therefore, we analyzed the dielectric response of all samples resorting to a Lorentz single oscillator description, justified by the close nearness in frequency with the TiO_2 transverse optical (TO) phonon mode in both the anatase and rutile phases.[45] In addition to the tail of the phonon modes, we assume that the carrier THz behavior of our polycrystalline samples is dominated by charge hopping, which can be thoroughly described using a phenomenological Drude-like response. A similar approach [Drude−Lorentz (DL) model] has been presented in the past on both polycrystalline and single crystal rutile samples using a more general harmonic oscillator model.[46] By using the DL model, the real $\varepsilon'(\omega)$ and the imaginary $\varepsilon''(\omega)$ parts of the dielectric function for a material with a single resonance can be explicitly expressed as[47]

$$\varepsilon'(\omega) = 1 + \frac{\omega_p{}^2(\omega_0{}^2 - \omega^2)}{(\omega_0{}^2 - \omega^2)^2 + \omega^2\gamma^2} \tag{5}$$

$$\varepsilon''(\omega) = \frac{\omega_p{}^2\gamma\omega}{(\omega_0{}^2 - \omega^2)^2 + \omega^2\gamma^2} \tag{6}$$

where ω_p is the plasma frequency, ω_0 is the phononic resonance frequency, and γ is the damping factor. We set a constant value ω_0 = 7.85 THz and ω_0 = 5.6 THz for the TO mode in all anatase and rutile samples, respectively,[42] regardless of the different synthesis routes and thermal treatments.

Moreover, starting from the complex dielectric function one can extract the frequency-dependent real conductivity σ' using the expression

$$\sigma'(\omega) = \varepsilon_0\omega\varepsilon''(\omega) \tag{7}$$

where ε_o is the vacuum permittivity.

Using an in-house minimization program based on the nonlinear least-squares regression algorithm, we fit the experimental data extracted from THz measurements (after accounting for the voids and the mixed-phase percentages as previously explained) with eqs 5 and 6 and retrieve the DL coefficients ω_p and γ set as free parameters.

https://dx.doi.org/10.1021/acs.jpcc.0c07568
J. Phys. Chem. C 2020, 124, 23773−23783

This approach gives a consistent fit of the dielectric function (real and imaginary part) for all samples, as it is clearly shown in Figure 3. Data are shown as a function of frequency and plotted on a semilog scale to better highlight the nearness of the TO phononic modes. Amorphous samples are excluded by the fitting procedure and are shown for comparison purpose only.

Rutile samples show a pronounced oscillating behavior likely due to the effect of multiple internal reflections produced by the large impedance mismatch between the sample dielectric constant and air.

The DL parameters are self consistently extracted by the nonlinear regression algorithm within a moderate ($R^2 > 0.5$) coefficient of determination. The values of dielectric constant obtained from measurements with the retrieved DL parameters are listed in Table 3. According to eq 1, the error in the dielectric constant is given by the indetermination in the filling fraction value and in the amorphous phase percentage reported in Table 1.

Table 3. The Values of Dielectric Constant Obtained from Measurements, ε', and Extracted from Eq 4, ε'_{eff}, and the DL Parameters ω_p and γ Retrieved from the Fit of the THz Dielectric Response

sample	ε'	ε'_{eff}	$\omega_p/2\pi$ [THz]	$\gamma/2\pi$ [THz]
SGT	8.5	21 ± 2		
SGT-400-1	15	51 ± 5	55 ± 3	3.1 ± 0.1
SGT-400-3	16	53 ± 5	56 ± 3	3.6 ± 0.1
SGT-400-5	15	46 ± 4	53 ± 2	6.3 ± 0.1
SGT-600-1	16	48 ± 4	54 ± 2	2.1 ± 0.1
SGT-800-1	28	71 ± 5	47 ± 2	2.3 ± 0.1
HSGT	9.5	20 ± 2		
HSGT-400-1	15	41 ± 4	50 ± 2	3.3 ± 0.1
HSGT-400-3	15.5	42 ± 4	49 ± 2	4.5 ± 0.1
HSGT-400-5	15.5	40 ± 3	47 ± 2	1.6 ± 0.1
HSGT-600-1	16	38 ± 3	47 ± 2	3.9 ± 0.1
HSGT-800-1	36	78 ± 5	49 ± 2	4.0 ± 0.1

The retrieved real dielectric constant ε' is consistent for both anatase and rutile pellets with range of values reported in the literature on powdered samples.[48−50]

One can easily observe that, independently of the presence of acetylacetone, TiO_2 powders show an increasing dielectric response that follows the phase transition, whereas no change within the estimated error is observed with annealing temperature and time for samples having the same phase and belonging to the same sample series. The absence of a dependence on the annealing temperature, in particular, agrees with previous observations on thin films.[51] Nevertheless, within the anatase phase, the SGT samples present ε' values significantly larger (25%) than the ones retrieved for the HSGT samples. The opposite is observed in the rutile phase, where the HSGT-800-1 shows a dielectric value slightly higher (10%) than the SGT-800-1. This result suggests that the effect of the acetylacetonate ligand present in the hybrid dried gels is preserved in the heat-treated samples altering the electro-optical properties of the anatase polymorph but producing a minor effect after the phase transition to rutile.

Overall, the slightly larger dielectric functions calculated for the SGT-anatase than for the HSGT-anatase may also indicate that different close-lying and flat dispersed bands near the conducting band edge occur for the anatase polymorph, giving a stronger polaron effect in SGT samples and leading to a larger average static dielectric constant. A discernible difference between the plasma frequency values for the HSGT-anatase ($\omega_p/2\pi \approx 50$ THz) and SGT-anatase ($\omega_p/2\pi \approx 55$ THz) samples is seen, whereas no significant dependence on the annealing temperature and time is observed. Rutile phase samples instead show very similar values for ω_p and in line with what is observed in the anatase phase.

The damping factor γ measures the level of dielectric phononic absorption in each sample. Not surprisingly, the loss level remains reasonably constant in the polycrystalline samples, both in the anatase and rutile phases. Even if the different crystal phases have different symmetries, close stacking planes, slip directions, and available interstitial positions per unit cell,[52] all of them likely play no role in the lattice losses.

The parameters retrieval using the DL model allows us to estimate the charge carrier density, $N \approx \omega_p^2 \varepsilon_0 m^*/e^2$. A wide range of values was reported in the literature for the effective electron mass m^* in the different phases of TiO_2. Numbers vary between 1 and 10 m_0 and between 5 and 100 m_0 (m_0 is the electron mass) for anatase and rutile, respectively. This large discrepancy originates from the different sample quality, and it makes therefore a correct estimation of the carrier density very elusive. There is however a more general consensus on a polaronic enhancement of the effective mass in both phases because of the strong interaction of the carriers with optical phonons.[53] Therefore, to retrieve N, we assume that m^* is constant within samples having the same phase regardless of the preparation conditions and that the higher the polaronic character of the electron−phonon interaction, the larger is the effective mass value. Under these assumptions, we assigned an effective mass $m^* = m_0$ for anatase and $m^* = 10m_0$ for rutile.[38] It follows that samples having rutile phase (HSGT-800-1 and SGT-800-1) show N values an order of magnitude larger with respect to the anatase phase ($N \approx 7 \div 8 \times 10^{18}$ to be compared with $N \approx 4 \div 5 \times 10^{17}$). The evident increase in the electron number density is therefore correlated with the phase transition only.

Reported works on the intrinsic transport properties of anatase proved that the metallic transition occurs for charge carrier concentrations $\geq 10^{19}$.[38] For both SGT and HSGT pellets, the yielded N values are far smaller than the metallic transition condition, confirming the non-degenerate nature of electrical transport properties that we can reasonably extend to all anatase samples independently of their annealing temperature. On the contrary, for the rutile samples, the charge carrier density is close to the transition limit, which is consistent with the observed increase in the conductivity with the phase transition from anatase into rutile. This is clearly displayed in Figure 4, where the real conductivity σ' values extracted using eq 7 for polycrystalline pellets are reported in a frequency decade. For the sake of clarity, data are reported for the samples annealed for 1 h only. σ' values for the amorphous TiO_2 are also shown for comparison.

The oscillations observed in the rutile samples once again reflect the large impedance mismatch in the transmission measurements at the interface between the sample and air. In the anatase phase, samples show close values of conductivity, with only a slight difference in the frequency behavior observed between SGT and HSGT pellets. This is somewhat surprising since a significant Ti^{3+}-self doping was observed for HSGT and HSGT-400-1 samples.[7] However, the low stability in air of Ti^{3+}

https://dx.doi.org/10.1021/acs.jpcc.0c07568
J. Phys. Chem. C 2020, 124, 23773−23783

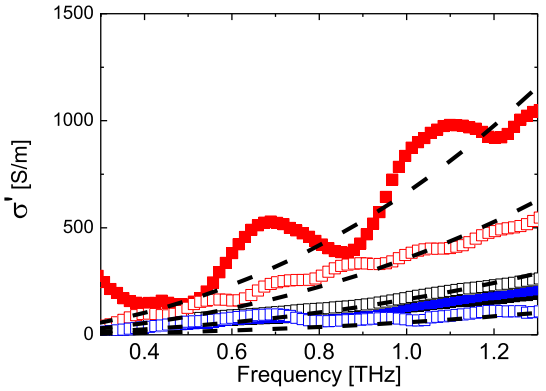

Figure 4. Conductivity σ' for HSGT (filled square symbols) and SGT (empty square symbols) pellets, under various annealing temperatures for 1 h. Red, blue, and black color code is used for rutile, anatase, and amorphous phases, respectively. Dashed curves represent data fits by applying the DL model to the polycrystalline samples.

as well as the possibility that the related oxygen vacancies defects may easily trap the excess electrons concurs in explaining the similarity in the transport properties of all anatase samples. It is worth noting that on the opposite, the values of electrical conductivity in anatase powders obtained from HSGT gel dried in vacuum and annealed in different atmospheres were found to be larger by more than 1 order of magnitude.[45] In that case, the formation of TiO_2/C bulk heterostructures was responsible for the excess charge carriers producing the observed increase in conductivity, rather than the presence of Ti^{3+}.

Notably, rutile samples present σ' values significantly larger than samples in the anatase phase. This evidence might be related to the limited amount of self-induced defects or carbon residuals induced by the acetylacetone present in the starting gel. Less defects might imply less carrier traps, leading to conductivity values that in HSGT-800-1 are up to 5 times greater than the anatase-bearing phases and to a more pronounced frequency dependence.

Moreover, the HSGT-800-1 pellet shows better conducting properties when compared with the corresponding SGT-800-1 pellet. A possible explanation might be assigned to the presence of a small amount of anatase (5%) as secondary phase in the SGT-800-1 sample. In this mixed phase, defects are generated at the interface between anatase and rutile, but they act as carrier trapping sites affecting the charge migration.[54]

The increase in σ' in both HSGT-800-1 and SGT-800-1 agrees with XPS data: samples annealed at 800 °C showed the highest values for both Ti LMM KE and extra-atomic relaxation energy. Indeed, R^{ea} is related to the polarization energy and is larger for conductors than for insulators. Thus, the trend in conductivity values obtained by THz-TDS is substantiated by the XPS results.

3.4. Electrostatic Model: "Bulk" Versus "Local" Dielectric Constant. According to Moretti,[24] considering the Jost cavity model,[55] the extra-atomic relaxation energy depends on the dielectric constant and the relationship is described by the equation

$$R^{ea} = C\left(1 - \frac{1}{\varepsilon'}\right)\frac{e^2}{r_0} \tag{8}$$

where R^{ea} is expressed in eV and $C = 7.2$ accounts for all numerical constants, $e = 1$ for a core hole state, and r_0 is the radius (in Å) of a spherical cavity centered on the emitting atom having ε' as the dielectric constant.

Assuming the same r_0 for the SGT and HSGT samples, the extra-atomic relaxation energy difference between annealed and amorphous samples retrieved from the XPS data (see Table 2) can be expressed, using eq 9, as

$$\Delta R^{ea}_{T-am} = \cos t\left(\frac{1}{\varepsilon'_{am}} - \frac{1}{\varepsilon'_{T}}\right) \tag{9}$$

where ε_{am}' and ε_{T}' are the dielectric constants of the amorphous and annealed samples, respectively. A similar method was used in the past to estimate from the difference of core-level BE shifts the local dielectric constant of different compounds, including Si,[56] AlN, and Al_2O_3.[57]

The Jost cavity model is valid, neglecting the nuclear relaxation so that one can assume that at optical frequencies ($\approx 10^{15}$ Hz) the dielectric constant equals the square of the refractive index ($\varepsilon' = n^2$) of the compound.

For a very high dielectric constant material like TiO_2 where $n \gg k$, one may assay to use eq 9 in order to have a qualitative guess on the relationship between local and bulk dielectric responses even at lattice vibration frequencies ($\approx 10^{13}$ Hz). The linear correlation observed in Figure 5 for ΔR^{ea}_{T-am}, calculated

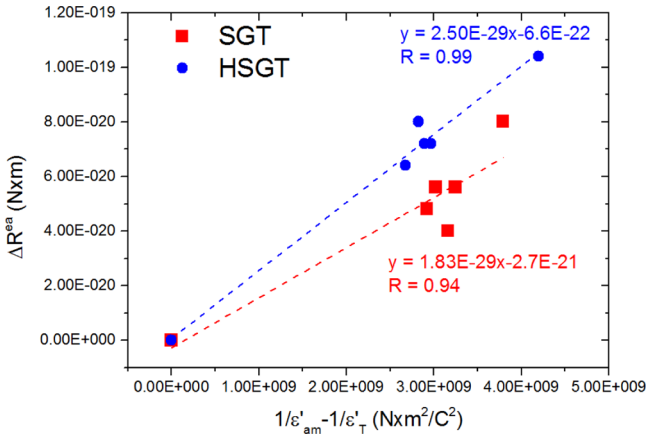

Figure 5. Extra-atomic relaxation energy difference (ΔR^{ea}_{T-am}) calculated between annealed and amorphous samples from XPS and X-ray-induced Auger electron spectroscopy data (Table 2) vs dielectric constant difference from THz-TDS spectroscopy (Table 3) for SGT (red squares) and HSGT (blue circles) samples at increasing temperatures.

by XPS data and plotted versus $\left(\frac{1}{\varepsilon_{am}} - \frac{1}{\varepsilon_{T}}\right)$, calculated from THz-TDS analysis, shows the validity of this assumption. Moreover, the data points of the two SGT and HSGT series fall in lines having different slopes, indicating that some diversity in the response certainly exists between them, despite the fact that the crystallite size, the crystalline phase fraction (Table 1), the chemical state of titanium, and the stoichiometry (Table 2) are almost identical. The main difference between the two series is the presence of the organic ligand in the synthesis procedure that affects the defectivity of annealed materials even if the organic phase is removed by the thermal treatment.

https://dx.doi.org/10.1021/acs.jpcc.0c07568
J. Phys. Chem. C 2020, 124, 23773−23783

A further clarification on the nature of defects is provided by a detailed analysis of photoelectron oxygen O 1s peak. Oxygen peak is multicomponent for all samples, indicating the presence of O in TiO_2 (BE = 530 eV), of a component ascribed to oxygen deficient regions (BE = 531 eV), and of adsorbed water (BE = 533 eV) (Figure S5).

If the percentage of the second component is plotted versus the annealing temperature (Figure 6), it is possible to observe that its content is always larger in HSGT than in SGT.

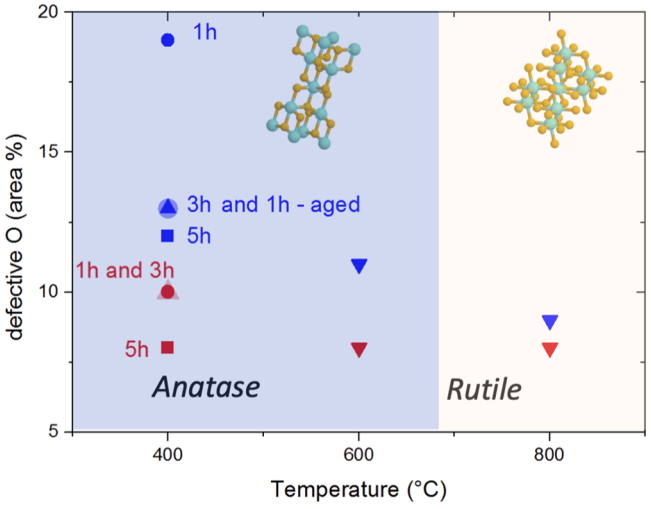

Figure 6. Percentage of defective oxygen from O 1s peak vs annealing temperature for HSGT (blue symbols) and SGT (red symbols) at different annealing times.

Moreover, in HSGT samples it dramatically decreases at 400 °C, increasing the annealing time, with a less pronounced reduction at 600 and 800 °C. All this points to a larger oxygen defectivity of such samples with respect to SGT ones, even after the thermal treatment.

Further confirmation of the presence of oxygen defectivity in HSGT-400-1 sample is provided by the XPS valence band region (Figure S6). The shape of the valence band allows distinguishing between anatase and rutile due to the different height of the two peaks located at about 5 and 7 eV, ascribed to O 2p non-bonding and O 2p bonding, respectively. In HSGT-400-1, at the lower BE side of the O 2p non-bonding peak, a small peak is detected. According to refs 2 and 13, this component might be due to partially filled Ti 3d non-bonding states, typical for Ti^{3+}-bearing titania. In this work, no evidence of such component is detected in the other samples.

Nevertheless, this neat difference in the defective oxygen content affects to a lesser extent the dielectric behavior retrieved using the THz TDS analysis, and it is almost not observed in the conductivity data, a possible indication that oxygen deficiency may modify the surface properties of TiO_2 chemical (HSGT) or particulate (SGT) gel-derived samples, without significantly perturbing the "bulk" properties.

4. CONCLUSIONS

A comprehensive study on the structure evolution of TiO_2 chemical (HSGT) and particulate (SGT) gels from amorphous to crystalline phases using XRD, SEM, XPS, and THz-TDS is presented, aiming to highlight how the different synthetic conditions lead to materials with different defect concentration and stability.

The XPS investigation proves that the introduction of the acetylacetonate ligand in the synthesis procedure increases the defectivity of annealed materials even after the organic phase is removed by thermal treatment.

This neat difference in behavior is present to a lesser extent in the THz dielectric response and conductivity data, a possible indication that oxygen deficiency may affect the surface properties of HSGT or SGT gel-derived samples, without significantly modifying the "bulk" properties. As a matter of fact, the defective structure is preserved in the heat-treated samples altering the electro-optical properties of the anatase polymorph while producing a minor effect after the phase transition to rutile. However, after the phase transition the HSGT rutile sample presents conductivity values significantly larger than samples in the anatase phase. In fact, the thermal treatment minimizes the effects of the presence of acetylacetone in the starting gel, reducing the number of oxygen vacancies or carbon residuals that can act as carrier charge traps.

It can be concluded that the formation and stabilization of a defective structure starting from the hybrid gel is mainly allowed in a specific and restricted range of annealing conditions.

This combined spectroscopic approach might significantly aid to enlighten the deep relationships between the nanostructure and the bulk charge carrier dynamics, which is fundamental to understand the role of defects in several applications of metal oxides, including photocatalysis and optoelectronics.

■ ASSOCIATED CONTENT

Supporting Information

The Supporting Information is available free of charge at https://pubs.acs.org/doi/10.1021/acs.jpcc.0c07568.

XRD patterns of all studied SGT and HSGT samples; Ti 2p and Ti LMM XP—high-resolution spectra of SGT and HSGT samples; example of O KLL X-ray-induced Auger peak recorded on HSGT-400-1 sample; kinetic energy differences and intensity ratios between O $KL_{23}L_{23}$ and O KL_1L_{23} evaluated as a function of temperature for SGT and HSGT series; O 1s peaks and XPS valence band spectra recorded on HSGT and SGT samples; and kinetic energy of O $KL_{23}L_{23}$ and O KL_1L_{23}, energy separation, and intensity ratio (PDF)

■ AUTHOR INFORMATION

Corresponding Authors

A. Andreone − *National Institute for Nuclear Physics, UdR Napoli, 80126 Napoli, Italy; Department of Physics, University of Naples Federico II, and CNR-SPIN, UOS Napoli, 80126 Napoli, Italy*; Email: antonello.andreone@unina.it

A. Rossi − *Department of Chemical and Geological Science, University of Cagliari, 09042 Monserrato, Cagliari, Italy*; orcid.org/0000-0002-5151-2634; Email: antonella.rossi@unica.it

Authors

C. Koral − *National Institute for Nuclear Physics, UdR Napoli, 80126 Napoli, Italy*

M. Fantauzzi − *Department of Chemical and Geological Science, University of Cagliari, 09042 Monserrato, Cagliari, Italy*

C. Imparato − *Department of Chemical, Materials and Production Engineering, University of Naples Federico II, 80125 Napoli, Italy*
G. P. Papari − *National Institute for Nuclear Physics, UdR Napoli, 80126 Napoli, Italy; Department of Physics, University of Naples Federico II, and CNR-SPIN, UOS Napoli, 80126 Napoli, Italy*
B. Silvestri − *Department of Chemical, Materials and Production Engineering, University of Naples Federico II, 80125 Napoli, Italy*
A. Aronne − *Department of Chemical, Materials and Production Engineering, University of Naples Federico II, 80125 Napoli, Italy;* orcid.org/0000-0002-2711-6789

Complete contact information is available at: https://pubs.acs.org/10.1021/acs.jpcc.0c07568

Author Contributions

C.K., M.F., and C.I. equally contributed to this investigation. The manuscript was written through contributions of all authors. All authors have given approval to the final version of the manuscript.

Notes

The authors declare no competing financial interest.

■ ACKNOWLEDGMENTS

The authors wish to express their deep gratitude to Prof. N. D. Spencer (Laboratory for Surface Science and Technology, ETH Zürich, Switzerland) for the access to the XPS facilities. Cossu is acknowledged for the technical assistance. Fondazione di Sardegna and University of Cagliari are gratefully acknowledged.

■ REFERENCES

(1) Chen, X.; Selloni, A. Introduction: Titanium Dioxide (TiO2) Nanomaterials. *Chem. Rev.* **2014**, *114*, 9281−9282.
(2) Sarkar, A.; Khan, G. G. The Formation and Detection Techniques of Oxygen Vacancies in Titanium Oxide-Based Nanostructures. *Nanoscale* **2019**, *11*, 3414−3444.
(3) Diebold, U. The Surface Science of Titanium Dioxide. *Surf. Sci. Rep.* **2003**, *48*, 53−229.
(4) Macwan, D. P.; Dave, P. N.; Chaturvedi, S. A Review on Nano-TiO2 Sol−Gel Type Syntheses and Its Applications. *J. Mater. Sci.* **2011**, *46*, 3669−3686.
(5) Kumar, S. G.; Rao, K. S. R. K. Polymorphic Phase Transition among the Titania Crystal Structures Using a Solution-Based Approach: From Precursor Chemistry to Nucleation Process. *Nanoscale* **2014**, *6*, 11574−11632.
(6) Sannino, F.; Pernice, P.; Imparato, C.; Aronne, A.; D'Errico, G.; Minieri, L.; Perfetti, M.; Pirozzi, D. Hybrid TiO2−Acetylacetonate Amorphous Gel-Derived Material with Stably Adsorbed Superoxide Radical Active in Oxidative Degradation of Organic Pollutants. *RSC Adv.* **2015**, *5*, 93831−93839.
(7) Aronne, A.; Fantauzzi, M.; Imparato, C.; Atzei, D.; De Stefano, L.; D'Errico, G.; Sannino, F.; Rea, I.; Pirozzi, D.; Elsener, B.; Pernice, P.; Rossi, A. Electronic Properties of TiO_2-Based Materials Characterized by High Ti^{3+} Self-Doping and Low Recombination Rate of Electron−Hole Pairs. *RSC Adv.* **2017**, *7*, 2373−2381.
(8) Pirozzi, D.; Imparato, C.; D'Errico, G.; Vitiello, G.; Aronne, A.; Sannino, F. Three-Year Lifetime and Regeneration of Superoxide Radicals on the Surface of Hybrid TiO2 Materials Exposed to Air. *J. Hazard. Mater.* **2020**, *387*, 121716.
(9) Imparato, C.; Iervolino, G.; Fantauzzi, M.; Koral, C.; Macyk, W.; Kobielusz, M.; D'Errico, G.; Rea, I.; Di Girolamo, R.; De Stefano, L.; Andreone, A.; Vaiano, V.; Rossi, A.; Aronne, A. Photocatalytic Hydrogen Evolution by Co-Catalyst-Free TiO2/C Bulk Heterostructures Synthesized under Mild Conditions. *RSC Adv.* **2020**, *10*, 12519−12534.
(10) Ou, G.; Xu, Y.; Wen, B.; Lin, R.; Ge, B.; Tang, Y.; Liang, Y.; Yang, C.; Huang, K.; Zu, D.; Yu, R.; Chen, W.; Li, J.; Wu, H.; Liu, L.-M.; Li, Y. Tuning Defects in Oxides at Room Temperature by Lithium Reduction. *Nat. Commun.* **2018**, *9*, 1302.
(11) Zhang, Y.; Xu, Z.; Li, G.; Huang, X.; Hao, W.; Bi, Y. Direct Observation of Oxygen Vacancy Self-Healing on TiO2 Photocatalysts for Solar Water Splitting. *Angew. Chem.* **2019**, *131*, 14367−14371.
(12) Hu, W.; Liu, Y.; Withers, R. L.; Frankcombe, T. J.; Norén, L.; Snashall, A.; Kitchin, M.; Smith, P.; Gong, B.; Chen, H.; Schiemer, J.; Brink, F.; Wong-Leung, J. Electron-Pinned Defect-Dipoles for High-Performance Colossal Permittivity Materials. *Nat. Mater.* **2013**, *12*, 821−826.
(13) Iatsunskyi, I.; Kempiński, M.; Nowaczyk, G.; Jancelewicz, M.; Pavlenko, M.; Załęski, K.; Jurga, S. Structural and XPS Studies of PSi/TiO2 Nanocomposites Prepared by ALD and Ag-Assisted Chemical Etching. *Appl. Surf. Sci.* **2015**, *347*, 777−783.
(14) Zhou, X.; Wierzbicka, E.; Liu, N.; Schmuki, P. Black and White Anatase, Rutile and Mixed Forms: Band-Edges and Photocatalytic Activity. *Chem. Commun.* **2019**, *55*, 533−536.
(15) Chen, X.; Burda, C. The Electronic Origin of the Visible-Light Absorption Properties of C-, N- and S-Doped TiO_2 Nanomaterials. *J. Am. Chem. Soc.* **2008**, *130*, 5018−5019.
(16) *Terahertz Spectroscopy: Principles and Applications*; Dexheimer, S. L., Ed.; Optical Science and Engineering; CRC Press: Boca Raton, 2008.
(17) Koral, C.; Ortac, B.; Altan, H. Terahertz Time-Domain Study of Silver Nanoparticles Synthesized by Laser Ablation in Organic Liquid. *IEEE Trans. Terahertz Sci. Technol.* **2016**, *6*, 525−531.
(18) Hendry, E.; Koeberg, M.; O'Regan, B.; Bonn, M. Local Field Effects on Electron Transport in Nanostructured TiO_2 Revealed by Terahertz Spectroscopy. *Nano Lett.* **2006**, *6*, 755−759.
(19) Mumtaz, M.; Ahsan Mahmood, M.; Rashid, R.; Ahmed, M.; Aslam Zia, M.; Ahmad, I. Investigation of the Optical and Conductive Properties of Antimony-Doped Titanium Dioxide Using Terahertz Time-Domain Spectroscopy. *Laser Phys. Lett.* **2018**, *15*, 105603.
(20) LaForge, J. M.; Cocker, T. L.; Beaudry, A. L.; Cui, K.; Tucker, R. T.; Taschuk, M. T.; Hegmann, F. A.; Brett, M. J. Conductivity Control of As-Grown Branched Indium Tin Oxide Nanowire Networks. *Nanotechnology* **2014**, *25*, 035701.
(21) Chen, T.; Hu, M.; Tan, L.; Wang, L.-C.; Li, L. Study on Switching Performance of VOx Thin Film in THz Band. *2010 10th IEEE International Conference on Solid-State and Integrated Circuit Technology*; IEEE: Shanghai, China, 2010; pp 1560−1562.
(22) Yu, C.; Zeng, Y.; Yang, B.; Donnan, R.; Huang, J.; Xiong, Z.; Mahajan, A.; Shi, B.; Ye, H.; Binions, R.; Tarakina, N. V.; Reece, M. J.; Yan, H. Titanium Dioxide Engineered for Near-Dispersionless High Terahertz Permittivity and Ultra-Low-Loss. *Sci. Rep.* **2017**, *7*, 6639.
(23) Wagner, C. D.; Gale, L. H.; Raymond, R. H. Two-Dimensional Chemical State Plots: A Standardized Data Set for Use in Identifying Chemical States by X-ray Photoelectron Spectroscopy. *Anal. Chem.* **1979**, *51*, 466−482.
(24) Moretti, G. Auger Parameter and Wagner Plot in the Characterization of Chemical States by X-ray Photoelectron Spectroscopy: A Review. *J. Electron Spectrosc. Relat. Phenom.* **1998**, *95*, 95−144.
(25) Wagner, C. D. Auger Lines in X-ray Photoelectron Spectrometry. *Anal. Chem.* **1972**, *44*, 967−973.
(26) Ascarelli, P.; Moretti, G. Ionicity of Metallic Oxide Surfaces on Metals as Observed by Auger (XPS) Spectroscopy. *Surf. Interface Anal.* **1985**, *7*, 8−12.
(27) Fantauzzi, M.; Atzei, D.; Elsener, B.; Lattanzi, P.; Rossi, A. XPS and XAES Analysis of Copper, Arsenic and Sulfur Chemical State in Enargites. *Surf. Interface Anal.* **2006**, *38*, 922−930.
(28) Fantauzzi, M.; Secci, F.; Sanna Angotzi, M.; Passiu, C.; Cannas, C.; Rossi, A. Nanostructured Spinel Cobalt Ferrites: Fe and Co Chemical State, Cation Distribution and Size Effects by X-ray Photoelectron Spectroscopy. *RSC Adv.* **2019**, *9*, 19171−19179.

(29) Papari, G. P.; Silvestri, B.; Vitiello, G.; De Stefano, L.; Rea, I.; Luciani, G.; Aronne, A.; Andreone, A. Morphological, Structural, and Charge Transfer Properties of F-Doped ZnO: A Spectroscopic Investigation. *J. Phys. Chem. C* **2017**, *121*, 16012−16020.
(30) *2007 Conference on Lasers & Electro-Optics: CLEO 2007; Baltimore, MD, USA, 6−11 May 2007; [Including PhAST 2007, Photonic Applications, Systems and Technologies Conference]*; Institute of Electrical and Electronics Engineers, Optical Society of America, Eds.; IEEE: Piscataway, NJ, 2007.
(31) Berrettoni, M.; Ciabocco, M.; Fantauzzi, M.; Giorgetti, M.; Rossi, A.; Caponetti, E. Physicochemical Characterization of Metal Hexacyanometallate−TiO_2 Composite Materials. *RSC Adv.* **2015**, *5*, 35435−35447.
(32) Carrus, M.; Fantauzzi, M.; Riboni, F.; Makosch, M.; Rossi, A.; Selli, E.; van Bokhoven, J. A. Increased Conversion and Selectivity of 4-Nitrostyrene Hydrogenation to 4-Aminostyrene on Pt Nanoparticles Supported on Titanium-Tungsten Mixed Oxides. *Appl. Catal., A* **2016**, *519*, 130−138.
(33) Villa, I.; Moretti, F.; Fasoli, M.; Rossi, A.; Hattendorf, B.; Dujardin, C.; Niederberger, M.; Vedda, A.; Lauria, A. The Bright X-ray Stimulated Luminescence of HfO_2 Nanocrystals Activated by Ti Ions. *Adv. Opt. Mater.* **2020**, *8*, 1901348.
(34) Venezia, A. M.; Rossi, A.; Duca, D.; Martorana, A.; Deganello, G. Particle Size and Metal-Support Interaction Effects in Pumice Supported Palladium Catalysts. *Appl. Catal., A* **1995**, *125*, 113−128.
(35) Fernández, A.; Caballero, A.; González-Elipe, A. R. Size and Support Effects in the Photoelectron Spectra of Small TiO2 Particles. *Surf. Interface Anal.* **1992**, *18*, 392−396.
(36) Luttrell, T.; Halpegamage, S.; Tao, J.; Kramer, A.; Sutter, E.; Batzill, M. Why Is Anatase a Better Photocatalyst than Rutile? - Model Studies on Epitaxial TiO2 Films. *Sci. Rep.* **2015**, *4*, 4043.
(37) Tighineanu, A.; Ruff, T.; Albu, S.; Hahn, R.; Schmuki, P. Conductivity of TiO2 Nanotubes: Influence of Annealing Time and Temperature. *Chem. Phys. Lett.* **2010**, *494*, 260−263.
(38) Tang, H.; Prasad, K.; Sanjinès, R.; Schmid, P. E.; Lévy, F. Electrical and Optical Properties of TiO2 Anatase Thin Films. *J. Appl. Phys.* **1994**, *75*, 2042−2047.
(39) Hendry, E.; Wang, F.; Shan, J.; Heinz, T. F.; Bonn, M. Electron Transport in TiO2 Probed by THz Time-Domain Spectroscopy. *Phys. Rev. B: Condens. Matter Mater. Phys.* **2004**, *69*, 081101.
(40) Turner, G. M.; Beard, M. C.; Schmuttenmaer, C. A. Carrier Localization and Cooling in Dye-Sensitized Nanocrystalline Titanium Dioxide. *J. Phys. Chem. B* **2002**, *106*, 11716−11719.
(41) Looyenga, H. Dielectric Constants of Homogeneous Mixture. *Mol. Phys.* **1965**, *9*, 501−511.
(42) Smith, N. Classical Generalization of the Drude Formula for the Optical Conductivity. *Phys. Rev. B: Condens. Matter Mater. Phys.* **2001**, *64*, 155106.
(43) Shimakawa, K.; Kasap, S. Dynamics of Carrier Transport in Nanoscale Materials: Origin of Non-Drude Behavior in the Terahertz Frequency Range. *Appl. Sci.* **2016**, *6*, 50.
(44) Němec, H.; Kužel, P.; Sundström, V. Far-Infrared Response of Free Charge Carriers Localized in Semiconductor Nanoparticles. *Phys. Rev. B: Condens. Matter Mater. Phys.* **2009**, *79*, 115309.
(45) Gervais, F.; Piriou, B. Temperature dependence of transverse- and longitudinal-optic modes in TiO_2 (rutile). *Phys. Rev. B: Solid State* **1974**, *10*, 1642−1654.
(46) Matsumoto, N.; Hosokura, T.; Kageyama, K.; Takagi, H.; Sakabe, Y.; Hangyo, M. Analysis of Dielectric Response of TiO2 in Terahertz Frequency Region by General Harmonic Oscillator Model. *Jpn. J. Appl. Phys.* **2008**, *47*, 7725−7728.
(47) Wegener, M. The Lorentz Oscillator Model and Beyond ... *Extreme Nonlinear Optics*; Advanced Texts in Physics; Springer-Verlag: Berlin/Heidelberg, 2005; pp 27−59.
(48) Mikami, M.; Nakamura, S.; Kitao, O.; Arakawa, H. Lattice dynamics and dielectric properties of TiO2 anatase: A first-principles study. *Phys. Rev. B: Condens. Matter Mater. Phys.* **2002**, *66*, 155213.
(49) Dou, M.; Persson, C. Comparative Study of Rutile and Anatase SnO2 and TiO2: Band-Edge Structures, Dielectric Functions, and Polaron Effects. *J. Appl. Phys.* **2013**, *113*, 083703.
(50) Wypych, A.; Bobowska, I.; Tracz, M.; Opasinska, A.; Kadlubowski, S.; Krzywania-Kaliszewska, A.; Grobelny, J.; Wojciechowski, P. Dielectric Properties and Characterisation of Titanium Dioxide Obtained by Different Chemistry Methods. *J. Nanomater.* **2014**, *2014*, 1−9.
(51) Kim, J. Y.; Jung, H. S.; No, J. H.; Kim, J.-R.; Hong, K. S. Influence of Anatase-Rutile Phase Transformation on Dielectric Properties of Sol-Gel Derived TiO2 Thin Films. *J. Electroceram.* **2006**, *16*, 447−451.
(52) Zhao, H.; Pan, F.; Li, Y. A Review on the Effects of TiO2 Surface Point Defects on CO2 Photoreduction with H2O. *J. Materiomics* **2017**, *3*, 17−32.
(53) Forro, L.; Chauvet, O.; Emin, D.; Zuppiroli, L.; Berger, H.; Lévy, F. High Mobility N-type Charge Carriers in Large Single Crystals of Anatase (TiO2). *J. Appl. Phys.* **1994**, *75*, 633−635.
(54) Choudhury, B.; Choudhury, A. Oxygen Defect Dependent Variation of Band Gap, Urbach Energy and Luminescence Property of Anatase, Anatase−Rutile Mixed Phase and of Rutile Phases of TiO2 Nanoparticles. *Phys. E* **2014**, *56*, 364−371.
(55) Jost, W. Diffusion and Electrolytic Conduction in Crystals (Ionic Semiconductors). *J. Chem. Phys.* **1933**, *1*, 466−475.
(56) Hirose, K.; Kihara, M.; Kobayashi, D.; Okamoto, H.; Shinagawa, S.; Nohira, H.; Ikenaga, E.; Higuchi, M.; Teramoto, A.; Sugawa, S.; Ohmi, T.; Hattori, T. X-ray Photoelectron Spectroscopy Study of Dielectric Constant for Si Compounds. *Appl. Phys. Lett.* **2006**, *89*, 154103.
(57) Hirose, K.; Suzuki, H.; Nohira, H.; Ikenaga, E.; Kobayashi, D.; Hattori, T. Relationship between Optical Dielectric Constant and XPS Relative Chemical Shift of 1s and 2p Levels for Dielectric Compounds. *J. Phys.: Conf. Ser.* **2008**, *100*, 012011.

https://dx.doi.org/10.1021/acs.jpcc.0c07568
J. Phys. Chem. C 2020, 124, 23773−23783